

On the Origin of *A*-type Antiferromagnetism and Chiral Split Magnons in Altermagnetic α -MnTe

Mojtaba Alaei,^{1,2} Pawel Sobieszczyk,³ Andrzej Ptok,³ Nafise Rezaei,¹ Artem R. Oganov,¹ and Alireza Qaiumzadeh⁴

¹*Materials Discovery Laboratory, Skolkovo Institute of Science and Technology, Bolshoy Boulevard 30, bld. 1, Moscow 121205, Russia*

²*Department of Physics, Isfahan University of Technology, Isfahan 84156-83111, Iran*

³*Institute of Nuclear Physics Polish Academy of Sciences, Radzikowskiego 152, 31-342 Krakow, Poland*

⁴*Center for Quantum Spintronics, Department of Physics, Norwegian University of Science and Technology, NO-7491 Trondheim, Norway*

(Dated: November 20, 2024)

The origin of the *A*-type antiferromagnetic ordering—where ferromagnetic layers couple antiferromagnetically—in the semiconductor altermagnet α -MnTe has been a subject of ongoing debate. Experimentally, α -MnTe exhibits a nearest-neighbor in-plane ferromagnetic exchange interaction, whereas previous ab initio calculations predicted an antiferromagnetic interaction. In this Letter, we resolve this discrepancy by considering an expanded set of magnetic configurations, which reveals an FM in-plane exchange interaction in agreement with experimental findings. Additionally, we demonstrate that the 10th nearest-neighbor exchange interaction is directionally dependent, inducing a chiral splitting in the magnon bands, as recently observed experimentally. We further show that applying a compressive strain reverses the sign of the in-plane exchange interaction and significantly enhances the spin and chiral splittings of the electronic and magnonic bands, respectively. Our results highlight the critical importance of convergence in the number of magnetic configurations for complex spin interactions in antiferromagnetic materials.

Introduction— Antiferromagnetic (AFM) interactions give rise to a diverse range of AFM classes, ranging from different collinear to various exotic noncollinear and frustrated structures [1–3]. A class of nonrelativistic collinear antiferromagnetic systems with broken combined parity and time-reversal (PT) symmetry, resulting in lifted Kramers’ degeneracy, while preserving the combined crystal rotation and time-reversal symmetry, has recently been identified in various AFM materials both theoretically [4–26] and experimentally [27–33]. This class of spin-split collinear AFM materials has been termed altermagnetism. In altermagnets, despite the absence of net magnetization, the electronic (magnonic) band structures display direction-dependent spin (chiral) splitting within certain regions of the magnetic Brillouin zone.

α -MnTe is a near-room-temperature, centrosymmetric correlated AFM semiconductor with a hexagonal crystal structure [34–36], recently identified as a candidate for *g*-wave altermagnetism [27–29, 37]. This material exhibits pronounced magnetostrictive and piezomagnetic properties [38, 39]. The nearest-neighbor (n.n.) Mn-Mn bond is along the interlayer direction while the 2nd n.n. is the in-plane bond, see Fig. 1(a). Experimentally, it was shown that the system has an *A*-type AFM structure [34, 40–42], with in-plane ferromagnetic (FM) exchange interaction, $J_2 > 0$ [40, 42]. However, recent density functional theory (DFT) calculations show an AFM exchange interaction $J_2 < 0$ [43–45]. On the other hand, recent inelastic neutron experiment has also found a chiral splitting of magnon bands in this system [42].

In this Letter, using ab initio calculations to compute the total energy, we resolve the previous discrepancy

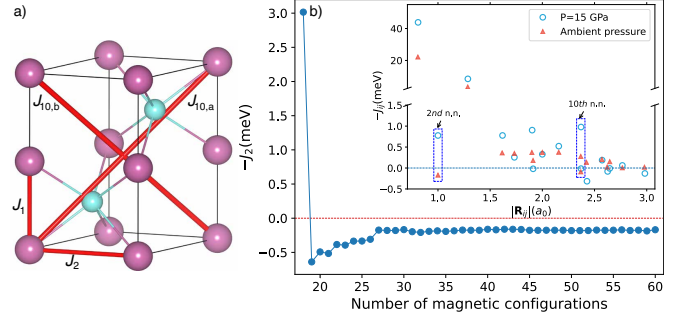


FIG. 1. (a) The crystal structure of α -MnTe. We present several important exchange interactions: the 10th n.n. interactions ($J_{10,a}$ and $J_{10,b}$) that lead to altermagnetism, as well as 1st. n.n. J_1 and 2nd n.n. J_2 . Large purple spheres represent Mn atoms and small cyan spheres represent Te atoms. (b) The 2nd nearest neighbor exchange interaction, J_2 , plotted against the number of magnetic configurations, starting from 18. Initially, J_2 is negative (AFM), but it transitions to positive (FM) and stabilizes as the number of configurations increases. Inset of (b) represents the Heisenberg exchange interactions at ambient pressure $P = 0$ and $P = 15$ GPa.

between DFT and experimental results. Our main finding, summarized in Fig. 1(b), shows that to find the correct sign for the in-plane exchange coupling J_2 , one needs to take into account many magnetic configurations. We also show that the 10th n.n. exchange interaction leads to chiral magnon splitting in this material. In addition, we demonstrate that applying compressive strain enhances both spin-split electronic bands and chiral-split magnon bands. Furthermore, the applied pressure changes the sign of J_2 , while still the magnetic ground state remains

collinear A -type AFM, offering new control over magnetic interactions.

Computational methods– To calculate the electronic band structures, the total energy, and consequently spin interactions, we use the projected augmented wave (PAW) method as implemented in the Vienna Ab initio Simulation Package (VASP) [46]. The plane wave expansion employs a cut-off energy of 550 eV. We apply the generalized gradient approximation (GGA) developed by Perdew, Burke, and Ernzerhof (PBE) to account for electron exchange-correlation energy [47]. Additionally, we include a Hubbard correction of $U = 4$ eV, as estimated in Ref. [48], to improve the treatment of electron-electron interactions.

To compute Heisenberg exchange interactions \tilde{J}_{ij} , between localized spins $\mathbf{S}_i = S\hat{\mathbf{S}}_i$, where $S = 5/2$ is the spin length and $\hat{\mathbf{S}}_i$ denotes the spin direction; we employ an implicit approach by fitting a classical Heisenberg model $\mathcal{H} = -\sum_{i<j} J_{ij}\hat{\mathbf{S}}_i \cdot \hat{\mathbf{S}}_j$, with $J_{ij} = S^2\tilde{J}_{ij}$; to the total energy derived from calculations of the electronic structure across numerous magnetic configurations [48–50]. For this, we compute exchange interactions up to the 16th n.n., allowing us to capture the chiral magnon band-splitting, accurately. To optimize computational efficiency, we select the minimal supercell that effectively captures all relevant exchange interactions. For this purpose, we apply the SUPERHEX method [51], recently introduced by some of us. Using SUPERHEX, we obtain a supercell with just 34 Mn atoms. In contrast, a conventional approach would require a much larger supercell of $5 \times 5 \times 4$, which contains 200 Mn atoms.

At ambient pressure, we use approximately 60 unique magnetic configurations and apply a least-squares fitting to the Heisenberg Hamiltonian model. Under a compressive pressure of 15 GPa, however, achieving convergence in exchange interactions requires about 120 magnetic configurations. In our DFT calculations, we neglect relativistic spin-orbit coupling effects to concentrate on the primary exchange interactions.

Spin-resolved electronic band structure– In altermagnets, Kramers’ degeneracy is lifted, leading to a momentum-dependent splitting of spin subbands in the electronic band structure. The left and right panels in Fig. 2 present the spin-resolved electronic band structure of bulk α -MnTe at ambient pressure and 15 GPa, respectively, along the L - Γ path in the Brillouin zone, where the material exhibits the largest spin splitting. We measure the nonrelativistic spin subband splitting at the $2/3L$ k-point to compare its behavior under different pressures. ΔV_1 represents the spin subband splitting of the first valence band, while ΔV_2 corresponds to the second valence band; see Fig. 2. We found a large spin split of $\Delta V_1 = 0.39$ eV and $\Delta V_2 = 0.96$ eV under ambient conditions consistent with recent experiments [27, 28]. On the other hand, at 15 GPa, ΔV_1 increases to 0.67 eV and

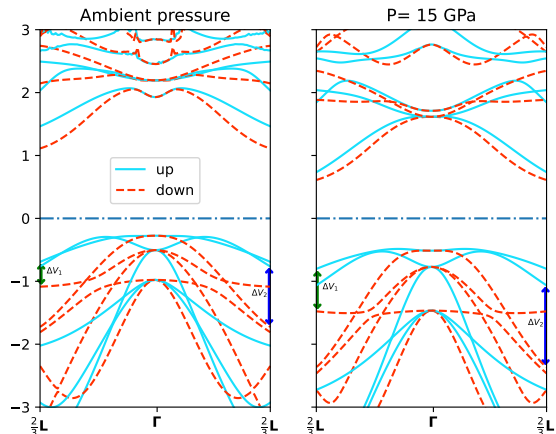


FIG. 2. Electronic band structure of altermagnetic semiconductor α -MnTe with g -wave symmetry of spin polarization in momentum space. The left and right panels show the spin-resolved band structure of bulk α -MnTe at ambient pressure and 15 GPa, respectively. ΔV_1 and ΔV_2 represent the spin subband splitting of the first and second valence bands, respectively.

ΔV_2 to 1.3 eV. This corresponds to about 70% increase in spin splitting of the first valence band and a 35% increase for the second valence band when the system is under a pressure of 15 GPa. We conclude that pressure enhances the nonrelativistic spin splitting in this material.

Heisenberg exchange interactions– In the inset of Fig. 1(b), we present the Heisenberg exchange interactions as a function of distance, derived from DFT calculations of the total energy at ambient pressure and 15 GPa. We present results up to the 16th n.n. Heisenberg exchange interactions, J_1 to J_{16} , see also Table I. It is clear that increasing the pressure strengthens the Heisenberg exchange interactions for most exchange couplings. This enhancement can be attributed to the reduction in bond lengths, which improves the overlap of electron wavefunctions and consequently increases electron hopping.

At ambient conditions, for the 2nd n.n., in-plane exchange interaction, our results predict an FM-type interaction, consistent with two experimental findings [40, 42], while previous ab initio studies report an AFM-type interaction [43–45]. Thus, the magnetic ground state is an A -type AFM as it was shown in experiments. It is worth noting that the $3d$ -orbital occupancy of the Mn^{2+} ions in α -MnTe is approximately 5.3, indicating it is not exactly at half-filling. This slight deviation from half-filling can facilitate FM exchange interactions between in-plane Mn ions, as the electron configuration allows for some degree of spin alignment.

We argue that this discrepancy between experiments and previous DFT calculations arise from using not enough number of magnetic configurations to map ab

initio total energy to the Heisenberg Hamiltonian. Figure 1(b) clearly shows that relying on only 18 magnetic configurations results in an incorrect AFM-type interaction for J_2 in our calculation as well. However, as we increase the number of magnetic configurations, the sign of exchange interaction switches to the correct FM-type interaction, highlighting the importance of verifying the convergence of exchange interactions with respect to the number of magnetic configurations in complex AFM systems. Although the sign of J_2 in our calculations is in agreement with the experimental measurements, its amplitude is smaller [40, 42]. We believe that this may arise from the limited number of Heisenberg exchange interactions chosen for fitting the experimental data. In addition, Fig. 1(b) shows that the sign of J_2 changes with pressure. Applying Monte Carlo solver to atomistic spin dynamics [52], we find that the magnetic ground state remains a collinear *A*-type AFM due to a large J_3 even though the sign of J_2 changes under applied pressure, see the Supplemental Material (SM) [53].

As we already mentioned, α -MnTe is a prototype of altermagnetic systems. Lifting the band degeneracy in both electronic and magnonic band structure of this material has been reported experimentally very recently [28, 42]. Due to its crystal symmetry, then we expect some Heisenberg exchange interactions exhibit two distinct interaction amplitudes in different directions. When considering exchanges up to the 16th n.n. in α -MnTe, we find that the 10th n.n. consists of two values, which we label them as $J_{10,a}$ and $J_{10,b}$. These two exchange interactions are illustrated in Fig. 1(a). In the figure, it is evident that the $J_{10,a}$ interaction is stronger than the $J_{10,b}$ interaction, due to the presence of Mn–Te bond connections in the $J_{10,a}$ interaction. The computed exchange interactions show that $J_{10,a}$ is stronger than $J_{10,b}$, see the inset of Fig. 1(b). Under pressure, the difference between $J_{10,a}$ and $J_{10,b}$ increases, with $J_{10,a}$ changing from -0.28 meV at the ambient pressure to -0.98 meV at 15 GPa, resulting an enhancement of AFM magnon band splitting.

Consistent with a very recent experiment, our calculations indicate that $J_{10,a}$ exhibits an AFM-type sign while $J_{10,b}$ shows an FM-type sign and thus lead to the chiral splitting of AFM magnon bands in altermagnetic α -MnTe, shown in the following. The pressure does not change the sign of them. We are not aware of any ab initio calculation for this exchange interaction.

Magnon dispersion and magnetic susceptibility—Finding Heisenberg exchange interactions, see Table I, we are able to compute magnon dispersion under both ambient conditions and under pressure as well as magnetic ground state and magnetic susceptibility. We use the following minimal spin Hamiltonian to describe the spin interactions in α -MnTe,

$$\mathcal{H} = - \sum_{i < j} J_{ij} \hat{\mathbf{S}}_i \cdot \hat{\mathbf{S}}_j - K \sum_i (\hat{\mathbf{S}}_i \cdot \hat{\mathbf{e}}_i)^2 - \mu_s h_0 \sum_i \hat{\mathbf{b}} \cdot \hat{\mathbf{S}}_i, \quad (1)$$

TABLE I. Comparison of Heisenberg exchange interactions, J_n (for $n = 1, \dots, 16$), in meV, calculated in this study at ambient pressure ($P = 0$) and high pressure ($P = 15$ GPa), with a recent experimental results [42].

J_n	$P = 0$	$P = 15$ GPa	Exp. [42]
J_1	-22.1816	-43.8556	-24.94
J_2	0.1686	-0.7762	0.75
J_3	-3.4239	-8.4657	-2.95
J_4	-0.3620	-0.7770	–
J_5	-0.3485	-0.2554	–
J_6	-0.3714	-0.9036	–
J_7	-0.1795	0.0185	–
J_8	-0.3734	-0.3274	–
J_9	-0.3770	-0.5216	–
$J_{10,a}$	-0.2772	-0.9780	-0.425
$J_{10,b}$	0.0907	0.0147	0.1381
J_{11}	-0.1361	0.3152	–
J_{12}	-0.2042	-0.1877	–
J_{13}	-0.0242	0.0810	–
J_{14}	-0.1523	0.0100	–
J_{15}	-0.0062	-0.0617	–
J_{16}	-0.0203	0.1297	–

where $K > 0$ is the single-ion uniaxial easy-axis magnetic anisotropy constant, $\hat{\mathbf{e}}_i$ is the magnetic anisotropy direction, and μ_s is the atomic magnetic moment. We assume a Zeeman-like interaction between localized magnetic moments and an external magnetic field with amplitude h_0 along the $\hat{\mathbf{b}}$ direction. The crystalline magnetic anisotropy, which arises from spin–orbit coupling, is very weak in α -MnTe. Due to its small magnitude, it cannot be reliably determined either experimentally or through ab initio calculations. For our analysis, we adopt a value of $K = 6.25$ meV [40, 43]. In collinear uniaxial AFM systems, magnons can have two chiral α and β eigenmodes, $\mathcal{H} = \sum_k (\omega_k^\alpha \alpha_k^\dagger \alpha_k + \omega_k^\beta \beta_k^\dagger \beta_k)$ [54]. In conventional \mathcal{PT} symmetric AFM systems, these two chiral modes are usually degenerate, $\omega_k^\alpha = \omega_k^\beta$. However, in altermagnets, the chiral magnon bands split [16] as was shown in a recent experiment on α -MnTe [42].

Figure 3 shows the magnon dispersion of α -MnTe in the absence and presence of pressure. Low energy magnons around the Γ symmetry point are degenerate while along the L- Γ -L symmetry path this degeneracy is broken. The pressure enhances the band splitting and also the magnon bandwidth. The spin-flip magnetic field in AFM systems is proportional to $\sqrt{J_1 K}$. Using dispersion relation calculations, we find a spin-flop magnetic field of $h_{\text{sf}} \approx 5.3$ T in the absence of the pressure while in the presence of the pressure it enhances to $h_{\text{sf}} \approx 7.6$ T, see the SM [53]. In addition, we compute the magnetic susceptibility of the system using Monte Carlo calculations in Fig. 4. The Néel temperature T_N can be readout from the maximum

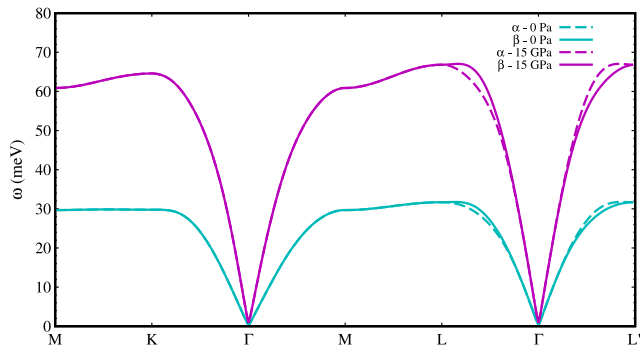


FIG. 3. Magnon dispersion relation of α -MnTe in the ambient conditions (green lines) and under a compressive pressure of 15 GPa (purple lines). In the absence of magnetic field, chiral α (dashed lines) and β (solid lines) magnon subbands are degenerate around the Γ symmetry point, while the chiral degeneracy is lifted along the L- Γ -L symmetry path. See the SM for magnon dispersions in the presence of a magnetic field [53].

of the longitudinal magnetic susceptibility. Within our calculations, we find $T_N \approx 250$ K in the absence of pressure and $T_N \approx 500$ K in the presence of pressure. Our calculations yield a lower Néel temperature compared to the experimental values, which are reported as 267 K for the thin film [28] and 307 K for the bulk material [42, 55]. This discrepancy is probably due to an underestimation of the exchange interaction parameter J_1 in our calculations.

Finally, from inverse magnetic susceptibility calculations, see the SM [53], we obtain the AFM Curie–Weiss temperature Θ via phenomenological Curie–Weiss law $\chi_z^{-1} \propto (T + \Theta)$ [56]. Under ambient conditions, we find $|\Theta| \approx 620$ K, which is slightly higher than the previous experimental values of 585 K reported in Refs. [57, 58]. Under applied pressure, however, $|\Theta|$ significantly increases to around 3100 K. These results are in agreement with the typical frustration index $|\Theta|/T_N \propto 2 - 5$ of unfrustrated 3d transition metals [56].

Concluding remarks– α -MnTe is an altermagnetic semiconductor with robust piezomagnetic properties, making it a promising candidate for spintronic applications. By resolving the in-plane Heisenberg exchange interaction J_2 discrepancy between the experimental findings and prior DFT calculations, we highlight the critical role of magnetic configurations in accurately modeling complex antiferromagnets. Furthermore, we identify $J_{10a(b)}$ as the primary driver behind the chiral magnon splitting in α -MnTe. Notably, applied pressure modulates both the sign and magnitude of the Heisenberg exchange interactions, enhancing spin polarization and chiral band splitting in both electronic and magnonic spectra. This work underscores the importance of detailed spin interaction analysis in advancing the physics of altermagnetic materials for next-generation spintronics technologies.

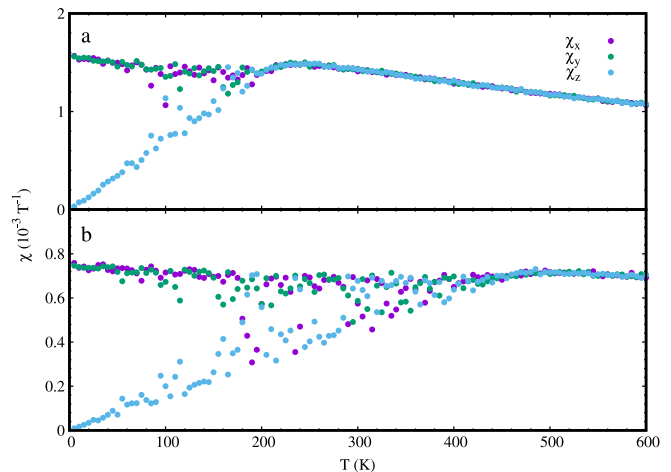


FIG. 4. Directional magnetic susceptibilities at the absence (a) and presence of pressure (b). In our atomistic simulations, we model a cubic system with dimensions of 10 nm \times 10 nm \times 10 nm, with periodic boundary conditions.

Acknowledgment– This work has been supported by the Research Council of Norway through its Centres of Excellence funding scheme, Project No. 262633, “QuSpin”. M.A., N.R., and A.R.O. supported by the Russian Science Foundation under Grant No. 19-72-30043.

-
- [1] V. Baltz, A. Manchon, M. Tsoi, T. Moriyama, T. Ono, and Y. Tserkovnyak, Antiferromagnetic spintronics, *Rev. Mod. Phys.* **90**, 015005 (2018).
 - [2] B. Rimmler, B. Pal, and S. Parkin, Non-collinear antiferromagnetic spintronics, *Nat. Rev. Mater.* (2024).
 - [3] A. Dal Din, O. Amin, P. Wadley, and K. Edmonds, Antiferromagnetic spintronics and beyond, *npj Spintronics* **2**, 25 (2024).
 - [4] Y. Noda, K. Ohno, and S. Nakamura, Momentum-dependent band spin splitting in semiconducting MnO₂: a density functional calculation, *Phys. Chem. Chem. Phys.* **18**, 13294 (2016).
 - [5] M. Naka, S. Hayami, H. Kusunose, Y. Yanagi, Y. Motome, and H. Seo, Spin current generation in organic antiferromagnets, *Nat. Commun.* **10**, 4305 (2019).
 - [6] S. Hayami, Y. Yanagi, and H. Kusunose, Momentum-dependent spin splitting by collinear antiferromagnetic ordering, *J. Phys. Soc. Jpn.* **88**, 123702 (2019).
 - [7] K.-H. Ahn, A. Hariki, K.-W. Lee, and J. Kuneš, Antiferromagnetism in RuO₂ as *d*-wave Pomeranchuk instability, *Phys. Rev. B* **99**, 184432 (2019).
 - [8] L. Šmejkal, R. González-Hernández, T. Jungwirth, and J. Sinova, Crystal time-reversal symmetry breaking and spontaneous Hall effect in collinear antiferromagnets, *Sci. Adv.* **6**, eaaz8809 (2020).
 - [9] L.-D. Yuan, Z. Wang, J.-W. Luo, E. I. Rashba, and A. Zunger, Giant momentum-dependent spin splitting in centrosymmetric low-*Z* antiferromagnets, *Phys. Rev. B* **102**, 014422 (2020).

- [10] S. A. Egorov, D. B. Litvin, and R. A. Evarestov, Antiferromagnetism-Induced Spin Splitting in Systems Described by Magnetic Layer Groups, *J. Phys. Chem. C* **125**, 16147 (2021).
- [11] I. I. Mazin, K. Koepernik, M. D. Johannes, R. González-Hernández, and L. Šmejkal, Prediction of unconventional magnetism in doped FeSb₂, *Proc. Natl. Acad. Sci. U.S.A.* **118**, e2108924118 (2021).
- [12] R. González-Hernández, L. Šmejkal, K. Výborný, Y. Yahagi, J. Sinova, T. Jungwirth, and J. Železný, Efficient Electrical Spin Splitter Based on Nonrelativistic Collinear Antiferromagnetism, *Phys. Rev. Lett.* **126**, 127701 (2021).
- [13] L. Šmejkal, J. Sinova, and T. Jungwirth, Emerging Research Landscape of Altermagnetism, *Phys. Rev. X* **12**, 040501 (2022).
- [14] L. Šmejkal, A. B. Hellenes, R. González-Hernández, J. Sinova, and T. Jungwirth, Giant and Tunneling Magnetoresistance in Unconventional Collinear Antiferromagnets with Nonrelativistic Spin-Momentum Coupling, *Phys. Rev. X* **12**, 011028 (2022).
- [15] L. Šmejkal, J. Sinova, and T. Jungwirth, Beyond Conventional Ferromagnetism and Antiferromagnetism: A Phase with Nonrelativistic Spin and Crystal Rotation Symmetry, *Phys. Rev. X* **12**, 031042 (2022).
- [16] L. Šmejkal, A. Marmodoro, K.-H. Ahn, R. González-Hernández, I. Turek, S. Mankovsky, H. Ebert, S. W. D'Souza, O. Šipr, J. Sinova, and T. Jungwirth, Chiral Magnons in Altermagnetic RuO₂, *Phys. Rev. Lett.* **131**, 256703 (2023).
- [17] L.-D. Yuan and A. Zunger, Degeneracy removal of spin bands in collinear antiferromagnets with non-interconvertible spin-structure motif pair, *Adv. Mater.* **35**, 2211966 (2023).
- [18] L.-D. Yuan, X. Zhang, C. M. Acosta, and A. Zunger, Uncovering spin-orbit coupling-independent hidden spin polarization of energy bands in antiferromagnets, *Nat. Commun.* **14**, 5301 (2023).
- [19] H. Yan, X. Zhou, P. Qin, and Z. Liu, Review on spin-split antiferromagnetic spintronics, *Appl. Phys. Lett.* **124**, 030503 (2024).
- [20] S. Bhowal and N. A. Spaldin, Ferroically Ordered Magnetic Octupoles in *d*-Wave Altermagnets, *Phys. Rev. X* **14**, 011019 (2024).
- [21] J. Sodequist and T. Olsen, Two-dimensional altermagnets from high throughput computational screening: Symmetry requirements, chiral magnons, and spin-orbit effects, *Appl. Phys. Lett.* **124**, 182409 (2024).
- [22] S.-W. Cheong and F.-T. Huang, Altermagnetism with non-collinear spins, *npj Quantum Mater.* **9**, 13 (2024).
- [23] A. Kimel, T. Rasing, and B. Ivanov, Optical read-out and control of antiferromagnetic Néel vector in altermagnets and beyond, *J. Magn. Magn. Mater.* **598**, 172039 (2024).
- [24] L. Bai, W. Feng, S. Liu, L. Šmejkal, Y. Mokrousov, and Y. Yao, Altermagnetism: Exploring New Frontiers in Magnetism and Spintronics, *Adv. Funct. Mater.* , 2409327 (2024).
- [25] T. Jungwirth, R. M. Fernandes, J. Sinova, and L. Šmejkal, Altermagnets and beyond: Nodal magnetically-ordered phases (2024), arXiv:2409.10034 [cond-mat.mtrl-sci].
- [26] T. Jungwirth, R. M. Fernandes, E. Fradkin, A. H. MacDonald, J. Sinova, and L. Šmejkal, From superfluid 3He to altermagnets (2024), arXiv:2411.00717 [cond-mat.mtrl-sci].
- [27] J. Krempaský, L. Šmejkal, S. W. D'Souza, M. Hailaoui, G. Springholz, K. Uhlířová, F. Alarab, P. C. Constantinou, V. Strocov, D. Usanov, W. R. Pudelko, R. González-Hernández, A. Birk Hellenes, Z. Jansa, H. Reichlová, Z. Šobáň, R. D. Gonzalez Betancourt, P. Wadley, J. Sinova, D. Kriegner, J. Minár, J. H. Dil, and T. Jungwirth, Altermagnetic lifting of Kramers spin degeneracy, *Nature* **626**, 517 (2024).
- [28] S. Lee, S. Lee, S. Jung, J. Jung, D. Kim, Y. Lee, B. Seok, J. Kim, B. G. Park, L. Šmejkal, C.-J. Kang, and C. Kim, Broken Kramers Degeneracy in Altermagnetic MnTe, *Phys. Rev. Lett.* **132**, 036702 (2024).
- [29] T. Osumi, S. Souma, T. Aoyama, K. Yamauchi, A. Honma, K. Nakayama, T. Takahashi, K. Ohgushi, and T. Sato, Observation of a giant band splitting in altermagnetic MnTe, *Phys. Rev. B* **109**, 115102 (2024).
- [30] O. Fedchenko, J. Minár, A. Akashdeep, S. W. D'Souza, D. Vasilyev, O. Tkach, L. Odenbreit, Q. Nguyen, D. Kutnyakhov, N. Wind, L. Wenthous, M. Scholz, K. Rossnagel, M. Hoesch, M. Aeschlimann, B. Stadtmüller, M. Kläui, G. Schönhense, T. Jungwirth, A. B. Hellenes, G. Jakob, L. Šmejkal, J. Sinova, and H.-J. Elmers, Observation of time-reversal symmetry breaking in the band structure of altermagnetic RuO₂, *Sci. Adv.* **10**, eadj4883 (2024).
- [31] S. Reimers, L. Odenbreit, L. Šmejkal, V. N. Strocov, P. Constantinou, A. B. Hellenes, R. Jaeschke Ubergo, W. H. Campos, V. K. Bharadwaj, A. Chakraborty, T. Deneuve, W. Shi, R. E. Dunin-Borkowski, S. Das, M. Kläui, J. Sinova, and M. Jourdan, Direct observation of altermagnetic band splitting in CrSb thin films, *Nat. Commun.* **15**, 2116 (2024).
- [32] M. Zeng, M.-Y. Zhu, Y.-P. Zhu, X.-R. Liu, X.-M. Ma, Y.-J. Hao, P. Liu, G. Qu, Y. Yang, Z. Jiang, K. Yamagami, M. Arita, X. Zhang, T.-H. Shao, Y. Dai, K. Shimada, Z. Liu, M. Ye, Y. Huang, Q. Liu, and C. Liu, Observation of Spin Splitting in Room-Temperature Metallic Antiferromagnet CrSb, *Adv. Sci.* , 2406529 (2024).
- [33] J. Ding, Z. Jiang, X. Chen, Z. Tao, Z. Liu, J. Liu, T. Li, J. Liu, Y. Yang, R. Zhang, L. Deng, W. Jing, Y. Huang, Y. Shi, S. Qiao, Y. Wang, Y. Guo, D. Feng, and D. Shen, Large band-splitting in *g*-wave type altermagnet CrSb (2024), arXiv:2405.12687 [cond-mat.mtrl-sci].
- [34] D. Kriegner, K. Výborný, K. Olejník, H. Reichlová, V. Novák, X. Marti, J. Gazquez, V. Saidl, P. Němec, V. V. Volobuev, G. Springholz, V. Holý, and T. Jungwirth, Multiple-stable anisotropic magnetoresistance memory in antiferromagnetic MnTe, *Nat. Commun.* **7**, 11623 (2016).
- [35] D. Bossini, M. Terschanski, F. Mertens, G. Springholz, A. Bonanni, G. S. Uhrig, and M. Cinchetti, Exchange-mediated magnetic blue-shift of the band-gap energy in the antiferromagnetic semiconductor MnTe, *New J. Phys.* **22**, 083029 (2020).
- [36] N. Devaraj, A. Bose, and A. Narayan, Interplay of altermagnetism and pressure in hexagonal and orthorhombic MnTe, *Phys. Rev. Mater.* **8**, 104407 (2024).
- [37] M. Chilcote, A. R. Mazza, Q. Lu, I. Gray, Q. Tian, Q. Deng, D. Moseley, A. Chen, J. Lapano, J. S. Gardner, G. Eres, T. Z. Ward, E. Feng, H. Cao, V. Lauter, M. A. McGuire, R. Hermann, D. Parker, M. Han, A. Kayani, G. Rimal, L. Wu, T. R. Charlton, R. G. Moore, and M. Brahlek, Stoichiometry-Induced Ferromagnetism in Altermagnetic Candidate MnTe, *Adv. Funct. Mater.* **34**, 2405829 (2024).
- [38] R. Baral, A. M. Abeykoon, B. J. Campbell, and B. A. Frandsen, Giant Spontaneous Magnetostriction in MnTe

- Driven by a Novel Magnetostructural Coupling Mechanism, *Adv. Funct. Mater.* **33**, 2305247 (2023).
- [39] T. Aoyama and K. Ohgushi, Piezomagnetic properties in altermagnetic MnTe, *Phys. Rev. Mater.* **8**, L041402 (2024).
- [40] W. Szuszkiewicz, E. Dynowska, B. Witkowska, and B. Hennion, Spin-wave measurements on hexagonal MnTe of NiAs-type structure by inelastic neutron scattering, *Phys. Rev. B* **73**, 104403 (2006).
- [41] D. Kriegner, H. Reichlova, J. Grenzer, W. Schmidt, E. Ressouche, J. Godinho, T. Wagner, S. Y. Martin, A. B. Shick, V. V. Volobuev, G. Springholz, V. Holý, J. Wunderlich, T. Jungwirth, and K. Vybórný, Magnetic anisotropy in antiferromagnetic hexagonal MnTe, *Phys. Rev. B* **96**, 214418 (2017).
- [42] Z. Liu, M. Ozeki, S. Asai, S. Itoh, and T. Masuda, Chiral Split Magnon in Altermagnetic MnTe, *Phys. Rev. Lett.* **133**, 156702 (2024).
- [43] I. I. Mazin, Altermagnetism in MnTe: Origin, predicted manifestations, and routes to detwinning, *Phys. Rev. B* **107**, L100418 (2023).
- [44] S. Mu, R. P. Hermann, S. Gorsse, H. Zhao, M. E. Manley, R. S. Fishman, and L. Lindsay, Phonons, magnons, and lattice thermal transport in antiferromagnetic semiconductor MnTe, *Phys. Rev. Mater.* **3**, 025403 (2019).
- [45] S. Rooj, J. Chakraborty, and N. Ganguli, Hexagonal MnTe with Antiferromagnetic Spin Splitting and Hidden Rashba–Dresselhaus Interaction for Antiferromagnetic Spintronics, *Adv. Phys. Res.* **3**, 2300050 (2024).
- [46] G. Kresse and D. Joubert, From ultrasoft pseudopotentials to the projector augmented-wave method, *Phys. Rev. B* **59**, 1758 (1999).
- [47] J. P. Perdew, K. Burke, and M. Ernzerhof, Generalized gradient approximation made simple, *Phys. Rev. Lett.* **77**, 3865 (1996).
- [48] Z. Mosleh and M. Alaei, Benchmarking density functional theory on the prediction of antiferromagnetic transition temperatures, *Phys. Rev. B* **108**, 144413 (2023).
- [49] M. Alaei and H. Karimi, A deep investigation of NiO and MnO through the first principle calculations and Monte Carlo simulations, *Electron. Struct.* **5**, 025001 (2023).
- [50] A. Szilva, Y. Kvashnin, E. A. Stepanov, L. Nordström, O. Eriksson, A. I. Lichtenstein, and M. I. Katsnelson, Quantitative theory of magnetic interactions in solids, *Rev. Mod. Phys.* **95**, 035004 (2023).
- [51] M. Alaei and A. R. Oganov, Optimizing Supercell Structures for Heisenberg Exchange Interaction Calculations (2024), arXiv:2410.14356 [cond-mat.mtrl-sci].
- [52] R. F. L. Evans, W. J. Fan, P. Chureemart, T. A. Ostler, M. O. A. Ellis, and R. W. Chantrell, Atomistic spin model simulations of magnetic nanomaterials, *J. Phys. Condens. Matter* **26**, 103202 (2014).
- [53] See Supplemental Material at URL-will-be-inserted-by-publisher for additional data.
- [54] S. M. Rezende, A. Azevedo, and R. L. Rodríguez-Suárez, Introduction to antiferromagnetic magnons, *J. Appl. Phys.* **126**, 151101 (2019).
- [55] G. Yumnam, D. H. Moseley, J. A. M. Paddison, C. Z. Suggs, E. Zappala, D. S. Parker, G. E. Granroth, G. D. Morris, M. M. H. Polash, D. Vashaee, M. A. McGuire, H. Zhao, M. E. Manley, B. A. Frandsen, and R. P. Hermann, Magnon gap tuning in lithium-doped MnTe, *Phys. Rev. B* **109**, 214434 (2024).
- [56] S. Mugiraneza and A. M. Hallas, Tutorial: a beginner’s guide to interpreting magnetic susceptibility data with the Curie-Weiss law, *Commun. Phys.* **5**, 95 (2022).
- [57] J. J. Banewicz, R. F. Heidelberg, and A. H. Luxem, High temperature magnetic susceptibilities of MnO, MnSe and MnTe, *J. Phys. Chem.* **65**, 615 (1961).
- [58] T. Komatsubara, M. Murakami, and E. Hirahara, Magnetic Properties of Manganese Telluride Single Crystals, *J. Phys. Soc. Jpn.* **18**, 356 (1963).

Supplemental Material for: *On the Origin of A-type Antiferromagnetism and Chiral Split Magnons in Altermagnetic α -MnTe*

In this Supplemental Material (SM), we provide additional plots for:

- 1- Magnon dispersion in the presence of an external magnetic field, Fig. S1;
- 2- Chiral splitting of magnon bands, Fig. S2;
- 3- Temperature dependence of the inverse longitudinal magnetic susceptibility, S3;
- 4- Effect of various exchange interactions on the magnetic ground state, Figs. S4, S5, and S6.

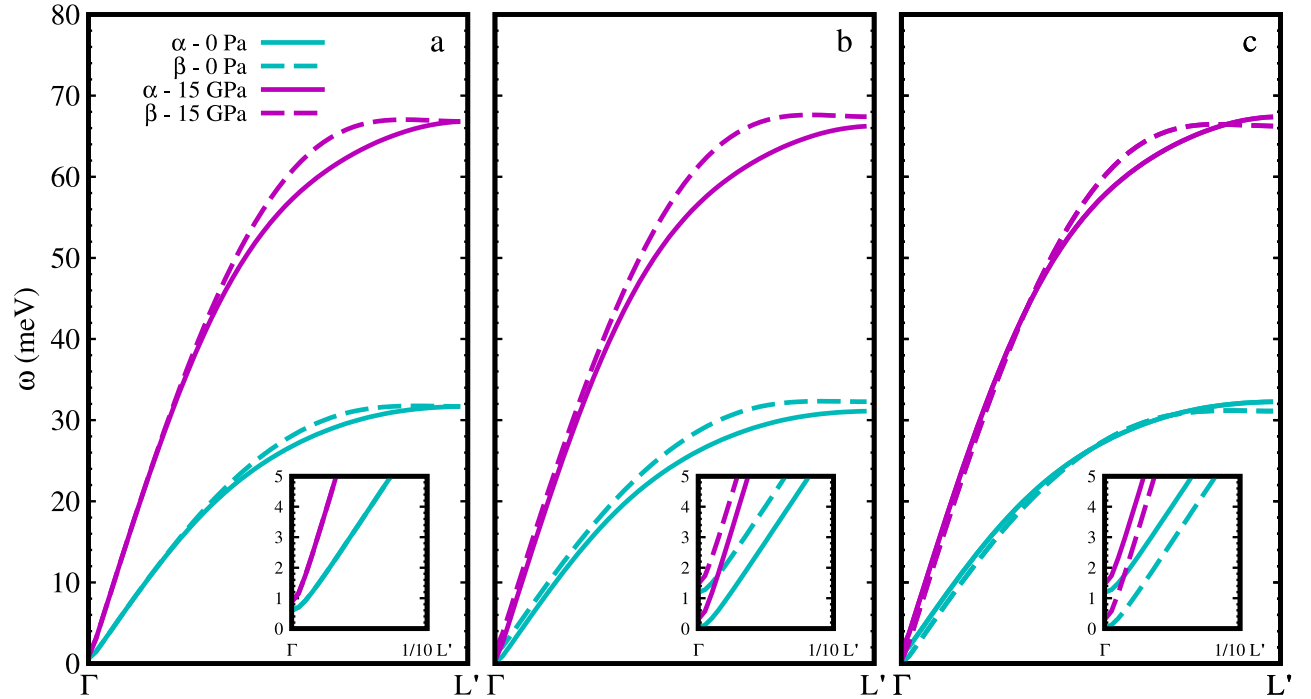


FIG. S1. Effect of external magnetic field on magnon dispersion relation of α -MnTe in the presence and absence of pressure. (a) in the absence of a magnetic field $h_0 = 0$. (b) $h_0 = -5$ T. (c) $h_0 = +5$ T. We find a spin-flop field $h_{sf} = 5.7$ T at $P = 0$ Pa and $h_{sf} = 7.6$ T at $P = 15$ GPa. It is worthy to note that in the presence of a magnetic field, two chiral magnon branches cross each other. Insets show the dispersions around the Γ symmetry point.

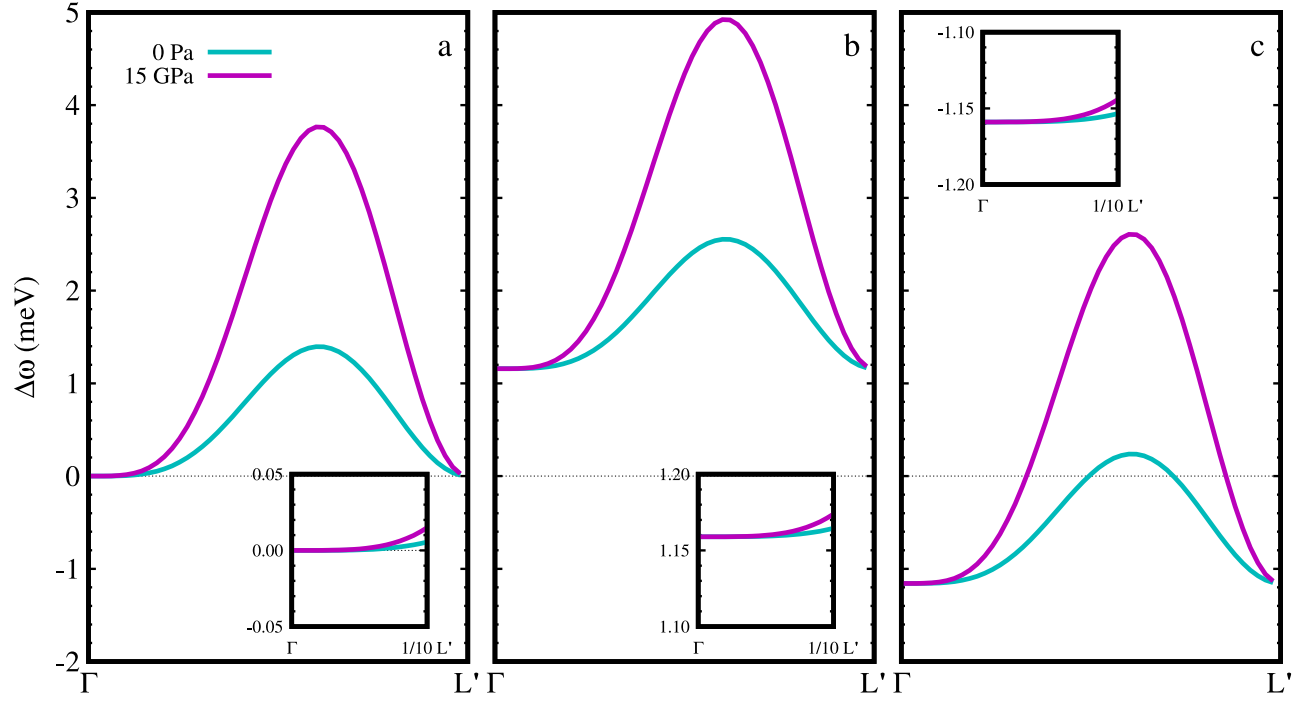


FIG. S2. Effect of magnetic field on splitting of chiral bands in the absence and presence of the pressure. (a) $h_0 = 0$. (b) $h_0 = -5$ T. (c) $h_0 = +5$ T. Insets show the splitting around the Γ symmetry point.

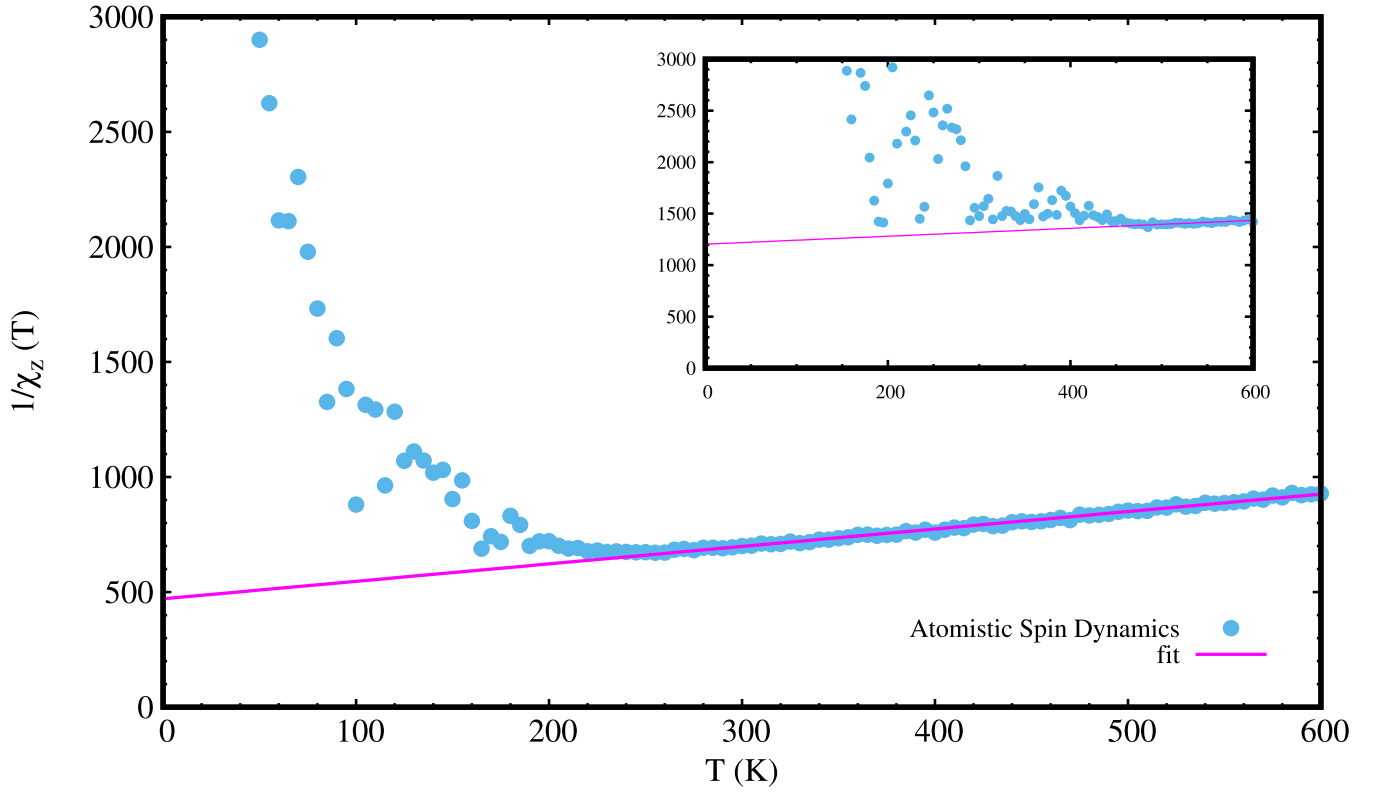


FIG. S3. Temperature dependence of the inverse longitudinal magnetic susceptibility, calculated using Monte Carlo simulations. The data are fitted with the antiferromagnetic Curie–Weiss law, $\chi_z^{-1} \propto (T + \Theta)$. Main plot: At ambient pressure ($P = 0$), the Curie–Weiss constant is $\Theta \approx -620$ K. Inset: Under compressive strain ($P = 15$ GPa), the constant increases to $\Theta \approx -3100$ K.

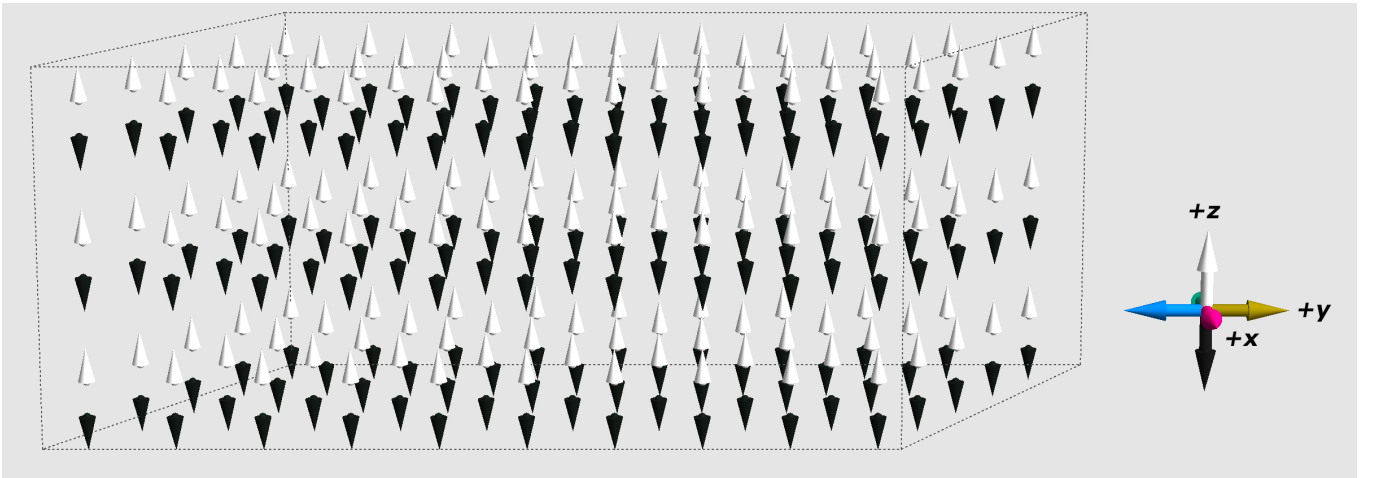


FIG. S4. Ground state magnetic configuration for α -MnTe at ambient conditions ($P = 0$) with only $J_1 < 0$ (AFM-type) and $J_2 > 0$ (FM-type) Heisenberg exchange interactions. System shows an A-type AFM ground state.

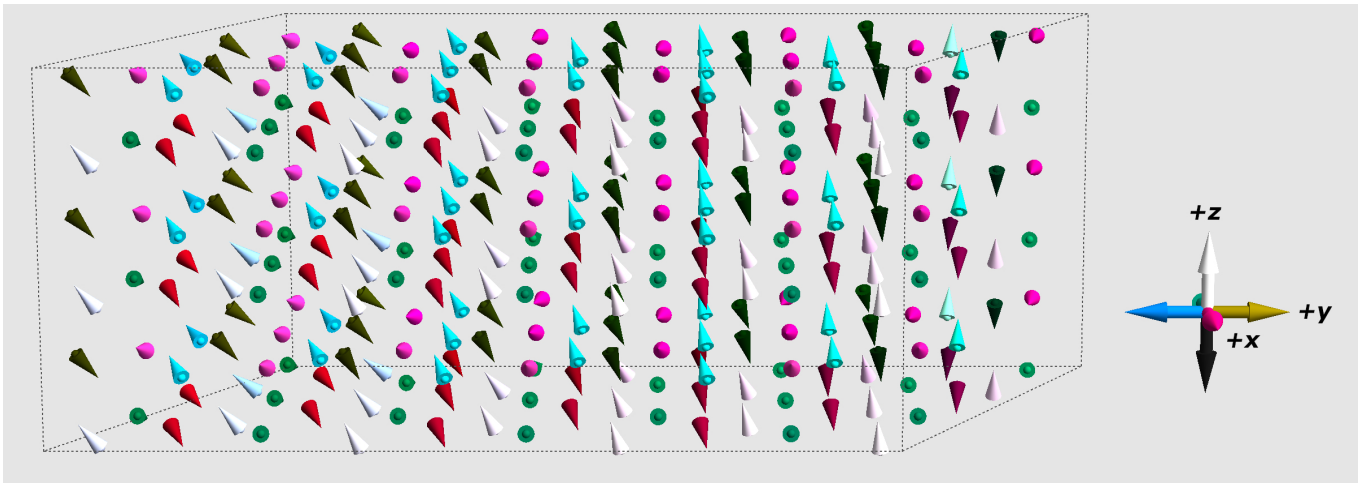


FIG. S5. Ground state magnetic configuration for α -MnTe under compressive strain ($P = 15$ GPa) with only $\{J_1, J_2\} < 0$, i.e., both interlayer and in-plane interactions are AFM type. System shows a frustrated AFM state.

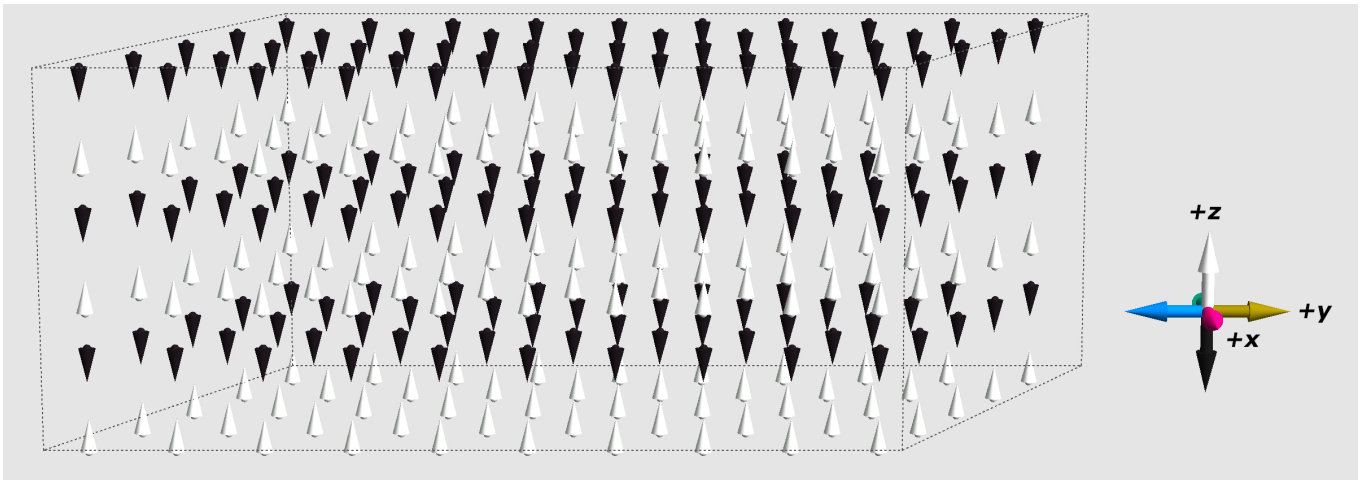


FIG. S6. Ground state magnetic configuration for α -MnTe under compressive strain ($P = 15$ GPa) with $\{J_1, J_2, J_3\} < 0$, i.e., all AFM type. $J_3 < 0$ stabilizes an *A*-type AFM ground state.